Surfactant-assisted hydrothermal synthesis of $CoMn_2O_4$ nanostructures for efficient supercapacitors

Pernapati Nagaraja[1,2] · Venkat Pamidi[3,4] · Ediga Umeshbabu[4] · T. Anirudh[3] · H. Seshagiri Rao[1,2] · G. Ranga Rao[1] · Ponniah Justin[2]

Abstract

Mixed transition metal oxides/spinels are excellent energy storage electrode materials that can deliver sizeable specific capacitance, excellent cyclic stability, and good rate capability than their single metal oxide analogues. Synthetic methods and strategies greatly influence materials' structure, morphology, and functionality. Among several strategies employed to improve the capacitance of metal oxides, the addition of surfactant is one of the simple strategies that help profoundly increase the electrode material's surface area/active sites. This study prepared a tetragonal spinel $CoMn_2O_4$ material using a simple hydrothermal approach by a surfactant, polyvinylpyrrolidone (PVP)-based morphological strategy. Electrochemical techniques such as cyclic voltammetry (CV) and galvanostatic charge/discharge cycling (GCD) were used to investigate the active material's energy storage properties. The structural and morphological properties were studied using XRD, SEM, and TEM techniques. The obtained $CoMn_2O_4$ material has unique and beautiful Indian borage shrub-like morphology. The unique morphology of $CoMn_2O_4$ material provided excellent electrochemical properties by virtue of its enhanced physico-chemical properties like pore size distribution, increased surface area, and many active sites for electrolyte ions that incurred large specific and areal capacitances. Further, the significant structural integrity provides extended cycling stability (~116% capacity retention) with high Coulombic efficiency of ~98% even after 6000 cycles without any dwindle in capacitance value. These fascinating features make $CoMn_2O_4$ a promising and optimistic pseudocapacitive electrode material.

Pernapati Nagaraja and Venkat Pamidi contributed equally to this work.

✉ G. Ranga Rao
grrao@iitm.ac.in

✉ Ponniah Justin
ponjustin@rgukt.in

1 Department of Chemistry and DST-Solar Energy Harnessing Centre, Indian Institute of Technology Madras, 600036 Chennai, India

2 Department of Chemistry, Rajiv Gandhi University of Knowledge Technologies, RK Valley, Kadapa 516330, Andhra Pradesh, India

3 Department of Metallurgical and Materials Engineering, Rajiv Gandhi University of Knowledge Technologies, RK Valley, Kadapa 516330, Andhra Pradesh, India

4 Helmholtz Institute Ulm (HIU) Electrochemical Energy Storage, Helmholtzstraße 11, 89081 Ulm, Germany

Introduction

Electrochemical energy storage technology has been one of the most rapidly growing research fields for the past two decades, as indicated by the number of publications [1–3]. These systems are essential in powering the rapid progress of portable electronic devices ranging from small gadgets such as smartwatches and mobile phones to digital cameras, laptops, uncrewed aerial vehicles, and consumer drones. Further, exponentially rising demand for electric vehicles in recent years and intermittent energy storage from renewable energy sources requires efficient energy storage systems with higher energy, more power, smaller volume, lighter weight, and high cycling life [4]. Due to the environmental impacts associated with the usage of fossil fuels and the growing need for large-capacity energy grids worldwide, researchers, policymakers, and the R&D industry turn their interest to energy storage systems [5]. Several new materials and architectures emerged in Li-ion batteries and supercapacitors in recent years. Nevertheless, their commercial success is limited by several structural

and kinetic matters [6]. For example, Li-ion battery technology has been used widely to power many portable gadgets by virtue of its high energy density (100–265 Wh/kg), which is limited by its low power density (< 1000 W/kg). On the contrary to this, supercapacitors are merited by their high-power density (> 10,000 W/kg) and longer operational time, which are essential for smart grid applications but are limited by low energy densities (4–10 Wh kg^{-1}) [2]. Therefore, new strategies, materials, and morphologies have been studied to achieve power and energy densities in a single entity.
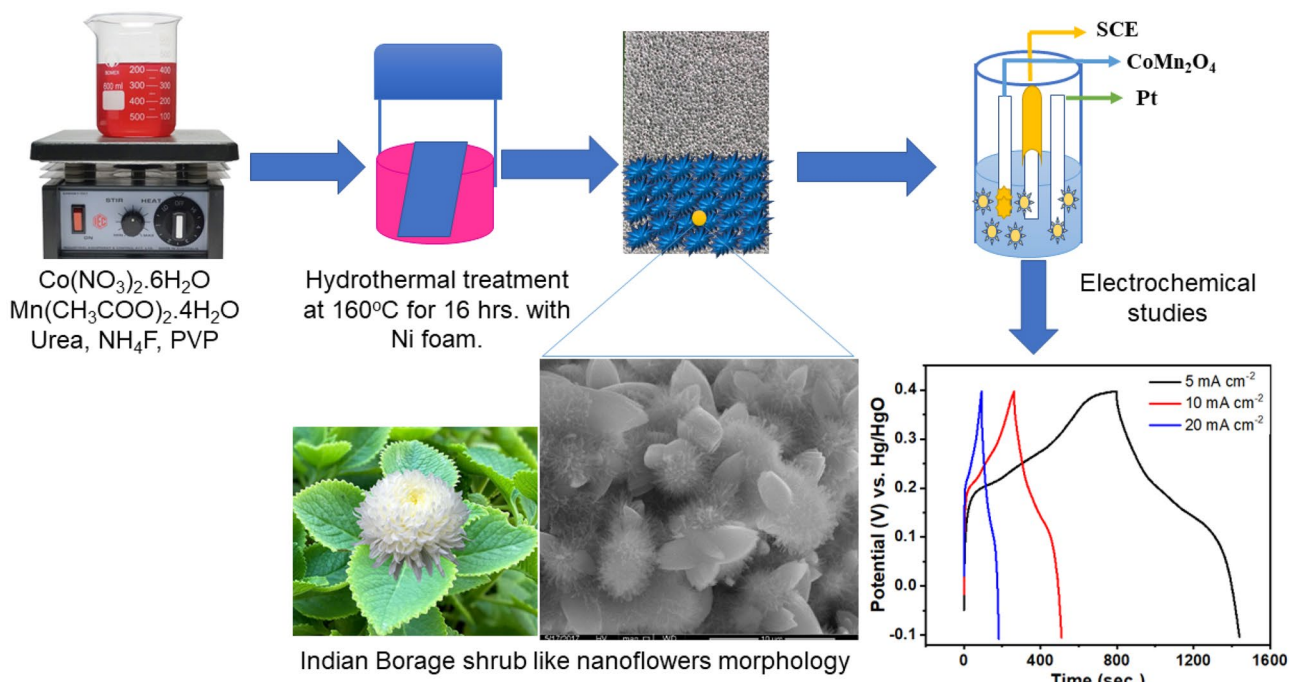
In this context, pseudocapacitors and hybrid capacitors gained tremendous attention in the last two decades with an exponential increase in publications. These efforts focus on finding the best suitable alternatives to address the high power and energy amalgamation in a single device. Recently, Srivastav et al. fabricated a uniform ribbon-like NiCo$_2$O$_4$-based all-solid-state supercapattery that delivered high energy (31 Wh kg^{-1}) and power density (13,003 W kg^{-1}) [7]. Pseudocapacitors store energy via a highly reversible faradaic reaction at the surface or near the surface of the active electrode along with double-layer capacitance [6]. The sum of these two charge storage mechanisms is termed "non-insertion capacitance" by Yuri and Reginald [8]. The carbonaceous materials derived from natural resources such as activated carbon (AC) from anthracite and nitrogen-doped activated carbon from palm flowers have controlled porosity with enlarged margins of surface areas. Recently, these carbonaceous materials have been fabricated and successfully evaluated as high-energy supercapacitors [9, 10]. On the other hand, transition metal oxides (TMOs) have also been extensively studied as successful pseudocapacitive materials due to their ease of fabrication, high theoretical specific capacitance, natural abundance, and environmental viability. In this era, several simple metal oxides (NiO, Co$_3$O$_4$, MnO$_2$, Fe$_3$O$_4$, V$_2$O$_5$) [11–15] and mixed metal oxides (NiCo$_2$O$_4$, ZnCo$_2$O$_4$, CoMn$_2$O$_4$) [16–18] were evolved as excellent pseudocapacitive materials and cheaper alternatives to RuO$_2$ based supercapacitors [19]. Recently, metal oxides such as NiO, Fe$_2$O$_3$, and Fe$_3$O$_4$ embedded in 2D carbonaceous nanosheets/flakes have been proved to be high-performance capacitive materials due to large mesopore volumes [20, 21]. Aparna et al. investigated bimetallic chalcogenides and oxynitrides as energy storage materials and concluded that bimetallic oxides, and oxynitrides can show better charge storage properties compared to chalcogenides (S, Se, and Te) [22, 23].

Since pseudocapacitance is an interfacial phenomenon, the mixed metal oxides with high surface area with a suitable pore-size distribution can facilitate the fast electrolyte ions accessibility throughout the material, and quicker reaction kinetics would offer higher capacitance. Among them, ternary metal oxides of the type MMn$_2$O$_4$ (M = Co, Ni, Zn) are the best suitable candidates due to the numerous advantages offered by manganese metal [24]. Nevertheless, these oxides suffer from poor electronic conductivity, limited surface area, and critical fabrication procedures. Since materials' surface properties profoundly influence their specific capacitance, it is essential to improve the surface area using new reaction strategies.

For instance, Ren et al. synthesized flower-like CoMn$_2$O$_4$ microspheres using a solvothermal technique and achieved a specific capacitance of 188 F g^{-1} in 1 M Na$_2$SO$_4$ at 1.1 V [25]. Syedvali et al. developed a simple surfactant free hydrothermal method to produce novel microstructures of rGO/Ni$_{0.3}$Co$_{2.7}$O$_4$ composite on a nickel foam, which exhibited excellent specific and areal capacitances of 1624 F g^{-1} and 2.37 F cm^{-2} at a current density of 2 A g^{-1} [26]. Luo et al. constructed urchin-like NiCo$_2$O$_4$ hollow microspheres by a self-template method that manifests a specific capacitance of 886 F g^{-1} at 1 A g^{-1} [27]. Tuning morphology by adding a minimum concentration of surfactant is one of the simple strategies to improve the surface area and hence the capacitance of the material [11, 19, 28, 29]. The addition of surfactants improves the physicochemical texture of the material, which provides better morphology with large pore volume and high specific surface area. All these characteristics influence the growth and nucleation of electroactive materials, which widens the electrode–electrolyte interface area and results in effective ion transport across the pore diameter of the electrode material. This enhances the material's specific capacitance, cyclic stability, and rate capability. For instance, Sandosh et al. followed a cetyltrimethylammonium bromide (CTAB)-assisted hydrothermal approach to prepare CoMn$_2$O$_4$ nanorods that showed a specific capacitance of 802 F g^{-1} at a current density of 1 A g^{-1} [30]. Padmanathan et al. synthesized mesoporous MnCo$_2$O$_4$ spinel oxide using a D-glucose-assisted solvothermal technique and achieved a specific capacitance of 346 F g^{-1} at 1 A g^{-1} [31].

This article reports the synthesis of CoMn$_2$O$_4$ nanostructures via a PVP surfactant-assisted hydrothermal approach. The PVP surfactant controlled the nucleation of cobalt manganite and resulted in beautiful nano *Chrysanthemum*-like flowers decorated on Indian borage shrubs-like morphology. This morphology specifically enhances the pseudocapacitance of the material due to enhanced surface area, good porosity, and hence accessibility to the electrolyte ions. The CoMn$_2$O$_4$ showed excellent pseudocapacitive properties with a high-specific capacitance of 1642 F g^{-1} and an areal capacitance of 4.92 F cm^{-2} at a current density of 3.3 A g^{-1}. Moreover, it displayed outstanding cycling stability and Coulombic efficiency due to the activation of many pores during the cycling process.

Scheme 1 The scheme that illustrates the preparation and electrochemical studies of $CoMn_2O_4$ material

Experimental section

Preparation of the $CoMn_2O_4$

Hydrothermal synthesis of spinel $CoMn_2O_4$ sample was reported in our previous work and can be found in Scheme 1 [18]. However, this work employed polyvinylpyrrolidone (PVP) as a surfactant and structure-directing agent. The amount of surfactant in this study was four times the metal salts used. We obtained a very high loading of active material on nickel foam, i.e., ~3 mg cm^{-2}.

Physical characterization

The phase purity and crystallite size were investigated using a powder X-ray diffractometer (XRD) (PANalytical instrument) fitted with a Cu Kα radiation source operating at 40 kV and 30 mA. The XRD pattern was recorded in the 2θ intervals ranging from 10 to 80° at a scan rate of 0.02° per min. Fourier-transform infrared spectroscopy (FT-IR) was recorded using a JASCO spectrometer in the 4000–400 cm^{-1} range. Micromeritics ASAP 2020 analyzer was used to carry out N_2 adsorption–desorption experiments on calcined $CoMn_2O_4$ sample. The surface area and pore size distribution were estimated using Brunauer-Emmet-Teller (BET) and Barret-Joyner-Halenda (BJH) methods. The microstructural examination of the calcined $CoMn_2O_4$ sample was performed using a field emission scanning electron microscope (FESEM, FEI Quanta 400) equipped with an energy dispersive spectroscopy (EDS) and transmission electron microscope (TEM, Technai-T20). The X-ray electron spectroscopy (XPS) measurements were carried out using Thermo scientific -NEXSA surface analysis with a micro-focused X-ray (400 μm, 72 W, 12,000 V) monochromatic Al-Kα source (hν = 1486.6 eV), a hemispherical analyzer, and a 128-channel plate detector. The C1s peak of carbon at 284.6 eV was used as a reference for the calibration of the binding energies.

Electrochemical characterization

The electrochemical properties of the as-prepared electrode were analyzed using a three-electrode configuration on an IVIUMstat electrochemical workstation using 2 M KOH as electrolyte. The platinum foil, Hg/HgO electrode (CHI Instruments), and as-prepared electrode (exposed area: 1 × 1 cm^2) were used as a counter, reference, and working electrodes, respectively. The active mass of $CoMn_2O_4$ electrode material on the Ni foam substrate is ~3 mg cm^{-2}. The electrochemical performance of the working electrode was evaluated by cyclic voltammetry (CV) and chronopotentiometry (CP). A potential window of −0.1–0.5 V and scan rates ranging from 5 to 20 mV s^{-1} were used to carry out CV tests. Similarly, a potential window of −0.1–0.4 V and different current densities ranging from 10 to 50 mA cm^{-2} were used to carry out CP tests.
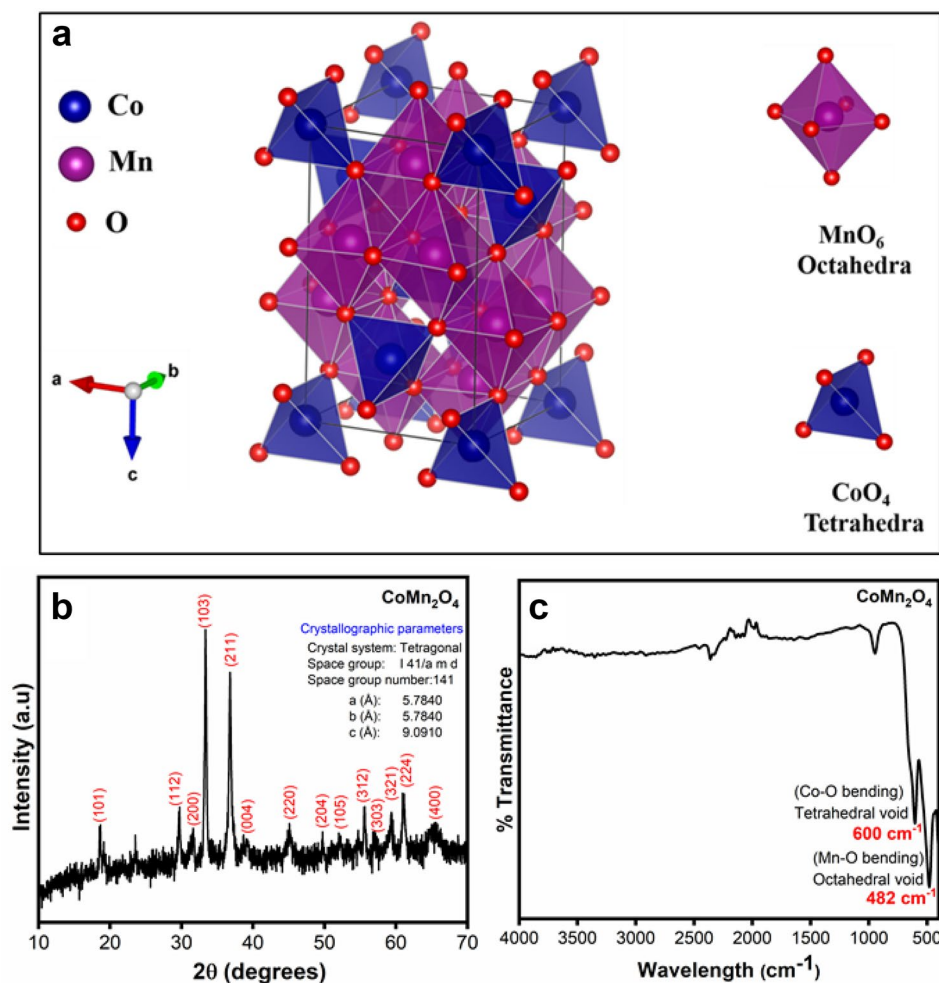
Results and discussion

Morphology and structural characterization

The fabrication process of the Indian borage shrub-like morphology of $CoMn_2O_4$ on Nickel foam is clearly illustrated in Scheme 1. In the preparation process, Ni foam is immersed in 350 mL of reaction solution that contains 2.10 g (20 mM) $Co(NO_3)_2$, 2.47 g (40 mM) $Mn(CH_3COO)_2$, 2.11 g (200 mM) Urea, 0.54 g (40 mM) NH_4F, and 3.28 g (80 mM) PVP surfactant. Hydrothermal heating of the reaction contents to 160 °C for 16 h (at a heating rate of 3° per minute) deposited cobalt manganese hydroxyl carbonate on Ni foam. The calcination of the obtained precursor at 400 °C evolves carbon dioxide with concomitant oxidation of Co^{2+} ions to Co^{3+} [32]. Eventually, the precursor molecules that are adsorbed on the interior surface of Ni foam undergo the Ostwald ripening process and finally blossom into beautiful chrysanthemum-like nanoflowers on Indian borage shrubs that is decorated on conductive Ni support [33]. The three-dimensional pore structure of Ni foam offers good support for the deposition of material, and the surfactant PVP added believed to be effectively controlled the agglomeration of nanoparticles during the nucleation process. Therefore, the growth of $CoMn_2O_4$ particles under the influence of PVP resulted in many nanoflowers on Indian borage shrub-like morphology. This morphology affords many pores/active sites for the transport of electrolyte ions into and out of the electrode material during the charge-discharging process. Further, nanoflowers that strongly adhere to the conductive support of Ni foam give a high degree of contact between the current collector and the active pores of the electrodes. That imparts great structural integrity over many cycles without suppressing its cyclic stability and pseudocapacitive performance.

The crystal structure of $CoMn_2O_4$, as displayed in Fig. 1a, reveals a spinel-type structure with a space group of Fd-3 m. In this structure, the cobalt and manganese ions (Co^{2+} and Mn^{3+}) dwell in the tetrahedral and octahedral symmetry, and O^{2-} occupies the faces leading to the formation of CoO_4 tetrahedron and MnO_6 octahedron. Powder X-ray diffraction

Fig. 1 **a** Crystallographic model of spinel $CoMn_2O_4$, where Co and Mn atoms occupy tetrahedral and octahedral sites in blue and orange, respectively. **b** Powder XRD pattern of $CoMn_2O_4$. **c** FT-IR spectrum of $CoMn_2O_4$

(XRD) was performed to analyse the sample's crystal structure and crystallite size. Figure 1b shows the XRD pattern of the $CoMn_2O_4$ sample. To avoid the strong impact of Ni foam substrate on the XRD pattern, the analysis was carried out on the product powder scratched from Ni foam, and a small amount of product collected from Teflon jar. The obtained diffraction peaks were matched with the JCPDS No. 18–0410, which validated the formation of the tetragonal spinel of the $CoMn_2O_4$ crystal. The crystallite size of the annealed sample was calculated using the Debye-Scherer formula [19]. The $CoMn_2O_4$ particles have an average crystallite size of ~36 nm. It is assumed that the surfactant has played a crucial role in controlling crystal growth, and it is also well-studied that surfactant molecules can stabilize particles. Stabilization of particles is essential to avoid particle agglomeration [25, 30].

The bonding properties of the synthesized spinel-type $CoMn_2O_4$ electrode material can be best evaluated using Fourier transform infrared (FT-IR) spectroscopic technique. The FT-IR spectrum of the material is shown in Fig. 1c and consists of two well-intense peaks at 600 and 482 cm^{-1} resulting from bending vibrations of Co–O (tetrahedral site) and Mn–O (octahedral site) [30, 34]. These characteristic peaks evidence the formation of a $CoMn_2O_4$ in a pure state and further support the XRD analysis.

Figure 2a shows the N_2 adsorption–desorption isotherms of the $CoMn_2O_4$ sample, which provides its surface textural characteristics. According to the IUPAC nomenclature, the sample exhibits mesoporous nature, which is confirmed by the presence of a type IV isotherm with an H3 hysteresis loop. The hysteresis loop of the $CoMn_2O_4$ sample in the relative pressure range of 0.4–1.0 confirms the presence of mesopores in the sample. However, the sudden increase in

the slope of the adsorption curve from 0.9 to 1.0 indicates the presence of a small fraction of macro-pores. The electrochemical performance of a sample depends on the number of active sites, which in turn depends on the specific surface area of the sample. The BET, the specific surface area of the $CoMn_2O_4$ sample was calculated and is reported as 62 $m^2\ g^{-1}$, which is higher than the earlier reported values for the $CoMn_2O_4$ sample [25, 35]. The BJH method was used to determine the pore size distribution of the sample using N_2 desorption curves (Fig. 2b). The $CoMn_2O_4$ sample exhibits a bimodal and narrow pore size distribution with peaks around 1.9 nm and 2.6 nm and a pore volume of 0.18 $cm^3\ g^{-1}$. The two pores with an average diameter of 2.25 nm originated from the needle-like morphology of nanoflowers nucleated under the influence of the PVP template while growing on Ni foam support. The limited pore size distribution (2–5 nm) with high-specific surface area and pore volume could offer an enormous number of active sites on the electrode that facilitate faster electron and ion transport, an essential prerequisite for high-rate practical supercapacitors.

Figure 3a–c shows the FE-SEM images of the $CoMn_2O_4$ sample at different magnifications. The microstructure consists of distinct morphological features such as a blend of chrysanthemum flowers embedded in Indian borage plant leaves and shrub-like structures, which are interconnected and uniformly grown on the surface of Ni foam substrate with a high degree of contact. These leaves are ~2–5-μm thick with a rough surface, and the shrubs have a round shape (~5 μm in diameter). The round shape arises from the self-assembling of many small needle-like structures with vast space between them. Morphologies like nanosheets [36, 37], hollow spheres [25, 38], and urchins [27, 39] were reported in the literature. This unique blend of
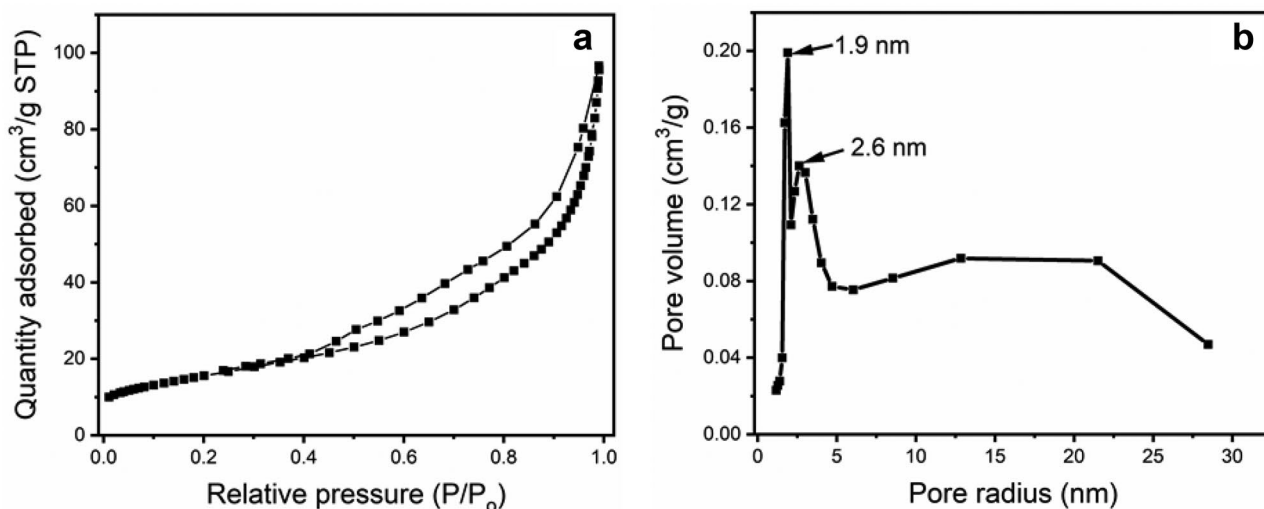

Fig. 2 **a** N_2 adsorption–desorption isotherms of $CoMn_2O_4$ sample. **b** BJH pore size distribution of the corresponding sample
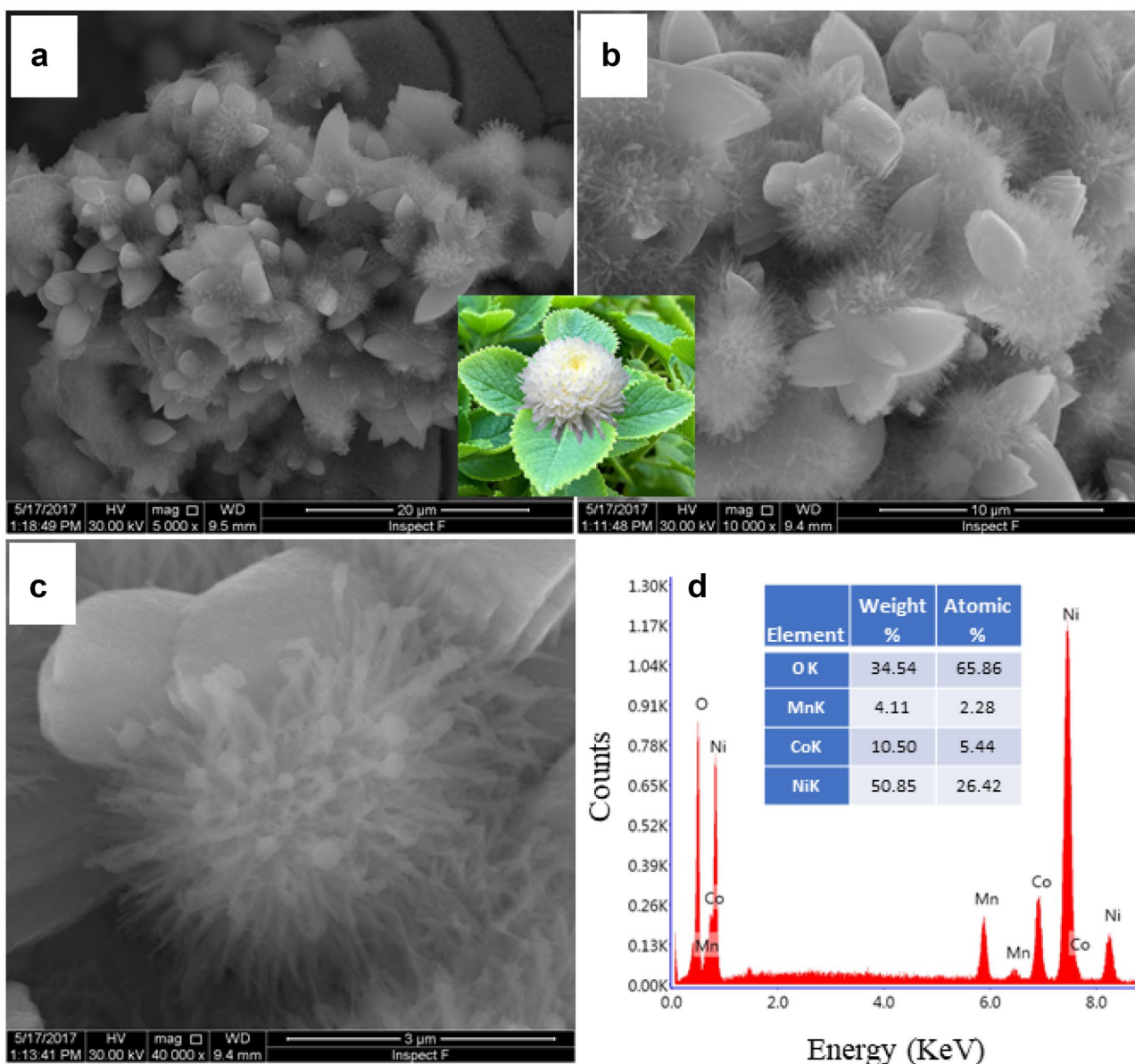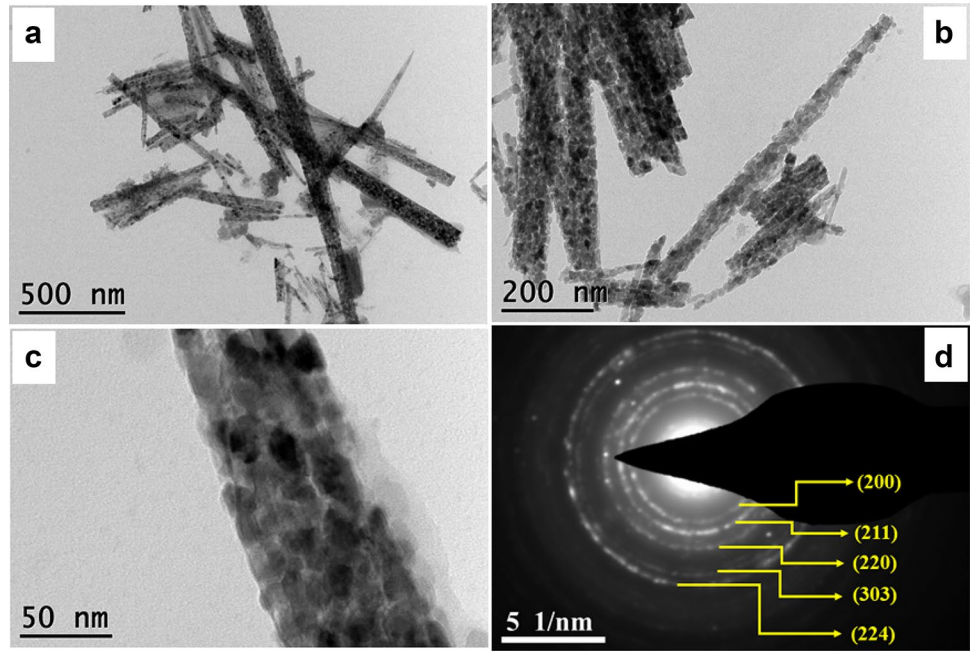
Fig. 3 **a–c** FESEM images of CoMn$_2$O$_4$ sample at different magnifications and **d** corresponding EDS analysis

morphological features is very stable, and well-organized microstructures of this kind help obtain superior electrochemical performance due to short ion diffusion lengths and easy electrolyte diffusion. Moreover, EDX analysis was also performed on the sample (Fig. 3d), which shows the elements Co, Mn, and O are uniformly distributed in the sample. Although Ni peaks are present in the EDX pattern, they belong to the Ni foam substrate. Figure 4 shows bright-field TEM images of the CoMn$_2$O$_4$ sample at different magnifications, taken from broken needle-like structures. It is observed that the sample is porous and polycrystalline in nature. Additionally, the selected area electron diffraction (SAED) revealed a dotted ring pattern (Fig. 4d), which is

attributed to the polycrystalline nature of the CoMn$_2$O$_4$ sample. The concentric rings correspond to (200), (211), (220), (303), and (224) planes of the CoMn$_2$O$_4$ sample, which are well agreed with the XRD pattern.

The elemental composition and electronic states of the CoMn$_2$O$_4$ spinel structure were evaluated by X-ray photoelectron spectroscopy (XPS), as shown in Fig. 5. The survey scan spectrum of the spinel (Fig. 5a) indicated the presence of elements like Co, Mn, and O, and a tiny small amount of C was used as reference. The XPS spectra consist of Co2p, Mn2p, and O1s (Fig. 5b–d) core-level spin–orbit peaks. The ratio of Co (11.32%) and Mn (22.92%) is clearly evidenced with XPS elemental analysis

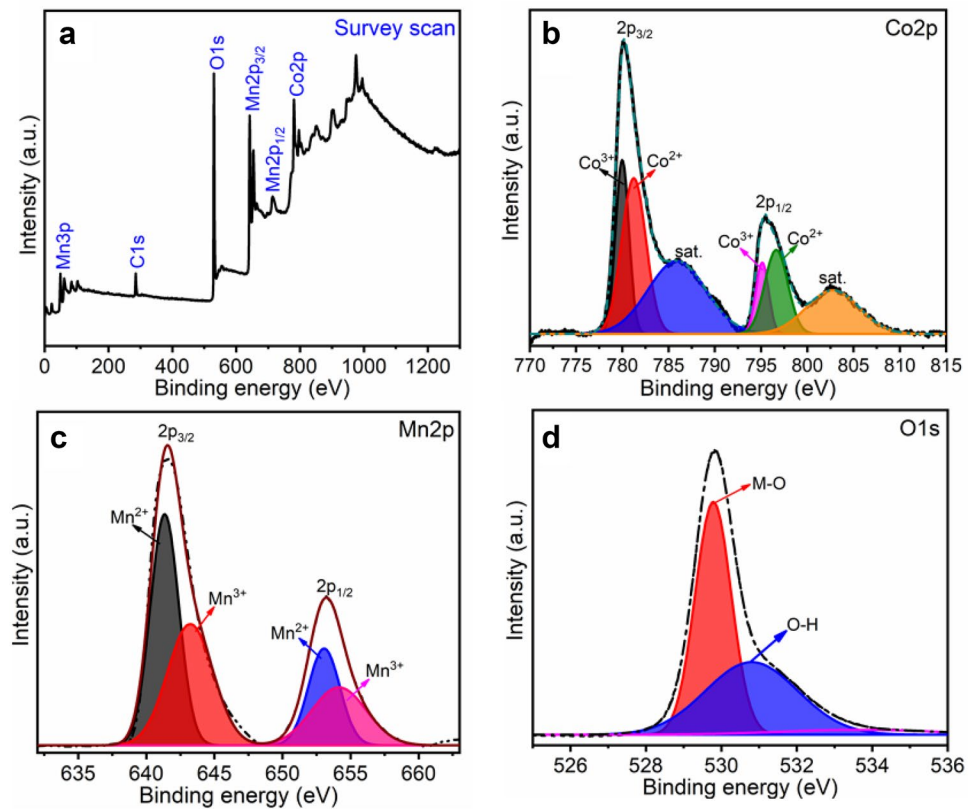**Fig. 4** **a–c** TEM images at different magnifications and **d** corresponding SAED pattern of CoMn₂O₄ sample

as 2.02 [32]. Figure 5b presents the Co2p spectrum consisting of doublet Co peaks 2p₃/₂ and Co2p₁/₂ at 780.01 and 795.11 eV, respectively. The energy splitting gap (ΔE) between di and trivalent Co ions is 15.1 eV, which is well-matched with many reports in the literature [35, 40]. The Co2p spectrum is fitted into four sub-peaks with binding energies of 781.32 and 796.59 eV for Co²⁺ and 780.01 and 795.11 eV for Co³⁺ states. The deconvolution of the Mn2p spectrum presented in Fig. 5c shows two prominent spin–orbit peaks located at 641.36 and 653.09 eV, corresponding to Mn2p₃/₂ and Mn2p₁/₂, respectively. The spin–orbit coupling difference between Mn 2p two peaks is

Fig. 5 **a** Survey scan spectrum of CoMn₂O₄; deconvoluted spectra of **b** Co 2p, **c** Mn 2p, and **d** O 1 s

about 11.25 eV which is a characteristic of Mn-based spinel materials. The $Mn2p_{3/2}$ and $Mn2p_{1/2}$ are further deconvoluted into sub-peaks positioned at 643.23 and 654.10 eV corresponding to Mn^{3+} and 641.36 and 653.09 eV for Mn^{2+} states [29]. The O1s deconvoluted spectrum is presented in Fig. 5d, which contains two intense peaks at 529.8 and 530.77 eV. These two peaks correspond to metal–oxygen (M–O) bonds and adsorbed OH$^-$ groups [41].

Electrochemical characterizations

The cyclic voltammograms of the $CoMn_2O_4$ electrode in 2 M KOH electrolyte in the potential window of -0.1 to 0.5 V (vs. Hg/HgO) at different scan rates (5, 10, 20 mV/s) are displayed in Fig. 6a. The pseudo-capacitive behavior of the electrode is confirmed by the non-rectangular shape of the CV curves. The oxidation states of the Co and Mn elements change in a quasi-reversible manner during forward and backward scans, which is confirmed by a pair of well-defined redox peaks in the CV curves. These redox peaks suggest that the $CoMn_2O_4$ electrode exhibits pseudo-capacitive behaviour, governed by the faradic reactions emerging from the charge transfer kinetics of the electrode. In addition, the current increases as the scan rate increases, but the shape of the CV curve changes very little, even at 20 mV s^{-1}. These characteristic features of the electrode material manifest fast faradic reactions and quick electronic/ionic transport even in the high-rate charge–discharge processes. It is further noted that drift in cathodic and anodic peak currents with scan rate is due to ohmic resistance and electric polarization behavior of $CoMn_2O_4$ electrode material [30]. The specific capacitance (C) values from CV curves at different scan rates are calculated using the following Eq. (1) [30, 42, 43].

$$C = \frac{\int idV}{2m.v.\Delta V} \quad (1)$$

Here, C = capacitance (F g^{-1}), $\int idV$ = integral area under CV curve, m = mass of electrode material (mg), ν = scan rate (mV s^{-1}), and ΔV = potential limit (V). For calculating specific capacitance, the integrated area under the CV curve is divided by the sweep rate (5–20 mV s^{-1}), the mass of active material (~3 mg), and the potential window (-0.1–0.5 V).

It is most commonly observed that the electrode material showing high capacitance (2216 F g^{-1}@5 mV s^{-1}) at a low scan rate attributes to the excellent adsorption/penetration of electrolyte ions (OH$^-$) in both outer and inner pores of the material due to sufficient transport time. While at higher scan rates, a low capacitance (862.8 F g^{-1}@20 mV s^{-1}) is observed due to insufficient time allowed for the ions to interact with the interfacial space of electrode material resulting in rapid electrode polarization [30, 42]. Further, the higher capacitance values obtained from the CV integral area are due to the electrode material's involvement of both surface redox and double-layer capacitance. The peak-to-peak separation increases when the scan rate increases, which is associated with the resistances and circuitous diffusion pathways within the porous textures of the electrode material. At higher scan rates, only outer regions can be accessed by the hydroxide ion, whereas outer and inner pore surfaces are utilised for charge propagation at lower scan rates. Generally, the diffusion coefficients of the hydroxide ion are half of the hydrogen ion. Accordingly, the mobility of the hydroxide ion is nearly half that of the hydrogen ion since the hydroxide ion is larger than the hydrogen ion. This also may be the reason for the peak-to-peak separation as we increase the scan rate in alkaline media. The faradaic reactions that are responsible for the pseudocapacitance of $CoMn_2O_4$ in an aqueous medium may be described by the following mechanism [25, 30, 36].
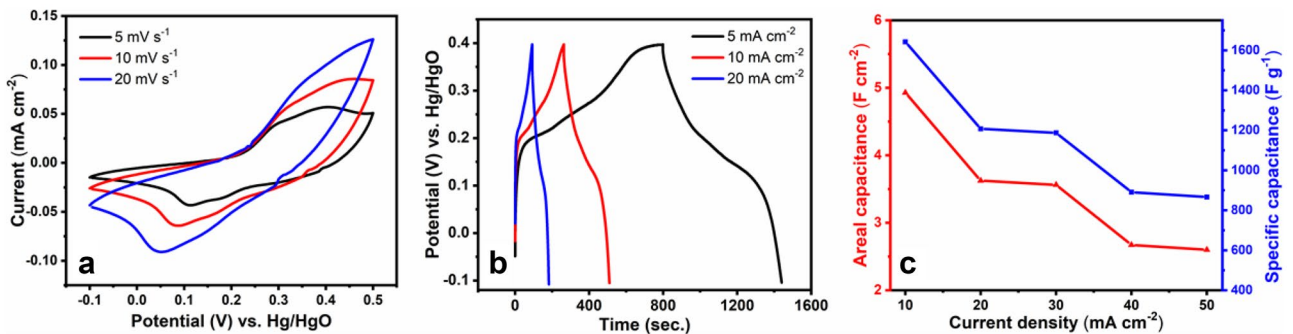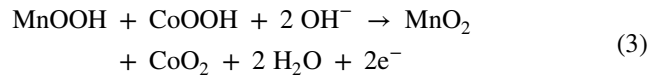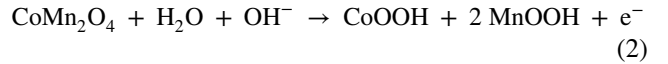
$$CoMn_2O_4 + H_2O + OH^- \rightarrow CoOOH + 2\,MnOOH + e^- \quad (2)$$

$$\begin{aligned} MnOOH + CoOOH + 2\,OH^- &\rightarrow MnO_2 \\ &+ CoO_2 + 2\,H_2O + 2e^- \end{aligned} \quad (3)$$

Fig. 6 **a** Cyclic voltammetry curves at different scan rates. **b** Charge–discharge curves at different current densities. **c** Areal and specific capacitance vs. current density

Chronopotentiometry (CP) was performed on the $CoMn_2O_4$ electrode at different current densities of 5, 10, and 20 mA cm^{-2} in the potential window of -0.1 to 0.4 V and presented in Fig. 6b. The slope of CP curves results from time dependency on potential and vice versa. The nonlinear nature of charge–discharge curves indicates the occurrence of faradic reaction at the electrode/electrolyte interface, demonstrating once again the pseudo-capacitive nature of the electrode in aqueous KOH, which is in good accordance with the CV data displayed in Fig. 6a. The electrode exhibited a much longer discharge time at a lower current density of 5 mA cm^{-2}. The effect of current density on the electrochemical performance of the electrode was studied by calculating the areal and specific capacitances at different current densities ranging from 10 to 50 mA cm^{-2}, and the results are summarized in Fig. 6c. The following equations were used in calculating areal and specific capacitances of the electrode:

$$C_s = \frac{I \times \Delta t}{m \times \Delta V} \tag{4}$$

$$C_a = \frac{I \times \Delta t}{s \times \Delta V} \tag{5}$$

where C_s means the specific capacitance (F g^{-1}), C_a is the areal capacitance (F cm^{-2}), I is the current (A), Δt is the discharge time (s), ΔV stands for the potential window (V), m is an active mass of the electrode (g), and s refers to surface area (cm^{-2}).

The electrode delivered areal and specific capacitances as large as 4.92, 3.62, 3.56, 2.67, and 2.60 F cm^{-2} and 1642, 1208, 1188, 890, and 866 F g^{-1} at current densities of 10, 20, 30, 40, and 50 mA cm^{-2} and 3.3, 6.6, 9.9, 13.2, and 16.5 A g^{-1}, respectively, which suggests that ~53% of initial capacitance is sustained even after very high charge–discharge rates. It is clearly evidenced that a decrease in specific capacitance with increased current density may arise due to the kinetic limitation process for the diffusion and transportation of charges. Mechanistically, it may be explained that the OH$^-$ ions move from the electrolyte to the electrode surface during the charging process. While discharging, a reverse movement of ions will occur. At low current densities, adequate time is provided for inserting ions onto the surface and interfacial regions of electrode material. On the contrary, at higher current densities, only limited time is available for the OH$^-$ ions to penetrate the electrode surface and interior pores, reducing the specific and areal capacitance of the electrode material [11, 26]. This mechanism of energy-storage at low and high current densities presented in Scheme 2. The areal and specific capacitance values obtained are higher than in many previous reports (Table 1). The superior behavior of the $CoMn_2O_4$ electrode material may be ascribed to (i) the increased surface area due to unique chrysanthemum nanoflower morphology, (ii) wide pore size distribution of nanoflower architectures, and (iii) due to shorter diffusion lengths, rapid ion/electron transportation over the nanostructured electrode material.

The reliability of supercapacitor devices is critically dependent upon their cyclic stability. Therefore, the cyclic stability of $CoMn_2O_4$ material was evaluated using chrono-amperometry at the current densities carrying from 10 to 40 mA cm^{-2} and back to 10 mA cm^{-2} for 6000 cycles as shown in Fig. 7a. The specific and areal capacitances were calculated at regular intervals (for every 50th cycle) and plotted in Fig. 7a. The first 1000 cycles were recorded at a current density of 10 mA cm^{-2} (3.3 A g^{-1}), and it is observed that C_s and C_a gradually increased from 788 to 1277 F g^{-1} and 1.82 to 4.00 F cm^{-2}, respectively. The large increment in capacitance can be attributed to the unique chrysanthemum nanoflower architecture with many of reachable pores as the number of cycle's increases. The specific/areal capacitance is higher than other morphologies, for instance, flower-like $CoMn_2O_4$ microspheres,

Scheme 2 The accessibility of OH$^-$ ions at a high scan rate (mainly on the surface regions) and low scan rate (both outer surface and inner pores)
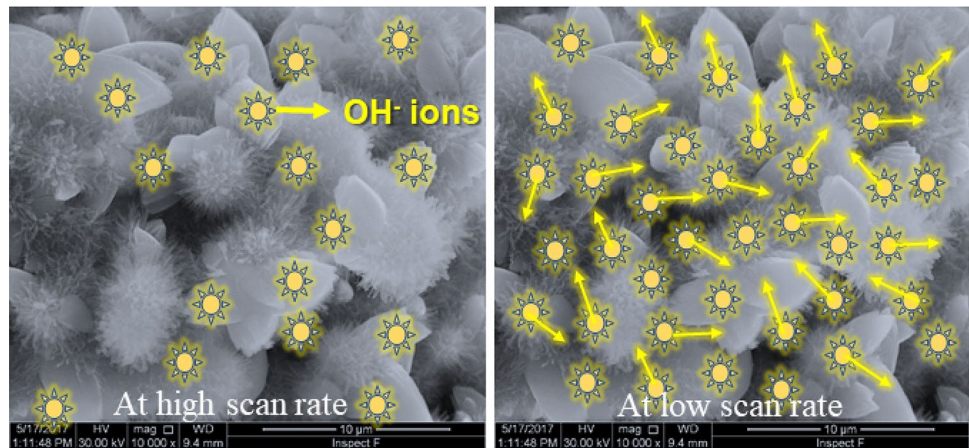
Table 1 Comparison of some CoMn₂O₄ electrodes with various morphologies and synthesis methods

Method	Morphology	Cs (F g⁻¹)	Cyclic stability	Ref
Hydrothermal	Urchin like	2484@2.8A/g	158% after 6000	18
Solvothermal	Microspheres	188@1A/g	93% after 1000	23
Hydrothermal	Nanorods	802@1A/g	87% after 5000	29
Hydrothermal	Nanoparticles	700@5 mV/s	60.5% after 2000	33
Hydrothermal	Nanosheets	910.1@1A/g	102% after 7000	34
Hydrothermal	Nanosheets	1529@2A/g	100% after 3000	35
Hydrothermal	Nanowires	2108@1A/g	100% after 4000	40
Co-precipitation	Microspheres	788@1A/g	67.6% after 4000	44
Hydrothermal	Nanoflowers	1642@3.3A/g	116% after 6000	This work

which showed 93% capacity retention after 1000 cycles [25], nanowires, and nanosheets of CoMn₂O₄ retained 100 and 102% of their initial capacitance, respectively [35, 44]. The increase in capacitance may be credited to the opening up (activation) of many internal pores during the cycling process, and hence, the increase in a number of active sites on the electrode surface [19]. Thus, this activation process is inevitable for any electrode, and it facilitates the access of a more significant number of active sites for the electrolyte ions in the system. Further increase in the current density to 20 mA cm⁻² (6.6 A g⁻¹), only a slight increment in capacitance is observed. If the current density is further doubled to 40 mA cm⁻² (13.2 A g⁻¹), a decrement trend is observed in both C_s and C_a. This trend may be explained as follows. At a low scan rate, sufficient time is allowed for the electrochemical process in both the inner pores and outer surface area of the electrode material [18]. However, at high current densities, only the electrolyte ions can actively utilize the outer surface region and no sufficient time to penetrate the inner pores. Hence, the capacitance follows a downtrend at higher current densities, and it is a commonly observed phenomenon in almost all supercapacitor electrodes, thus reported in most of the literature [25, 45, 46]. After completing 4000 cycles, the current densities were again decreased to 20 mA cm⁻² (6.6 A g⁻¹) for up to 5000 cycles and then further to 10 mA cm⁻² (3.3 A g⁻¹) from 5000 to 6000 cycles. Due to improved kinetics, an increment in capacitances is observed at these lower current densities. It is interesting to note that the capacitance of the CoMn₂O₄ electrode gradually increases at all current densities without any decrement. This suggests activating more and more active sites internally and externally throughout the material without any deterioration or structural change. This could be credited to the electrode material's unique morphology and structural integrity that incurs good cyclic stability and rate capability and the continuous increase in capacitance even after 6000 cycles. Additionally, the electrode maintained an impressively high average capacity retention (C_{ret}) of ~116% and a high Coulombic efficiency of ~98%, indicating it is a promising electrode material for high-performance supercapacitor applications. Thus, the PVP-assisted CoMn₂O₄ electrode exhibits attractive morphology and superior electrochemical performance than similar materials prepared without PVP due to high
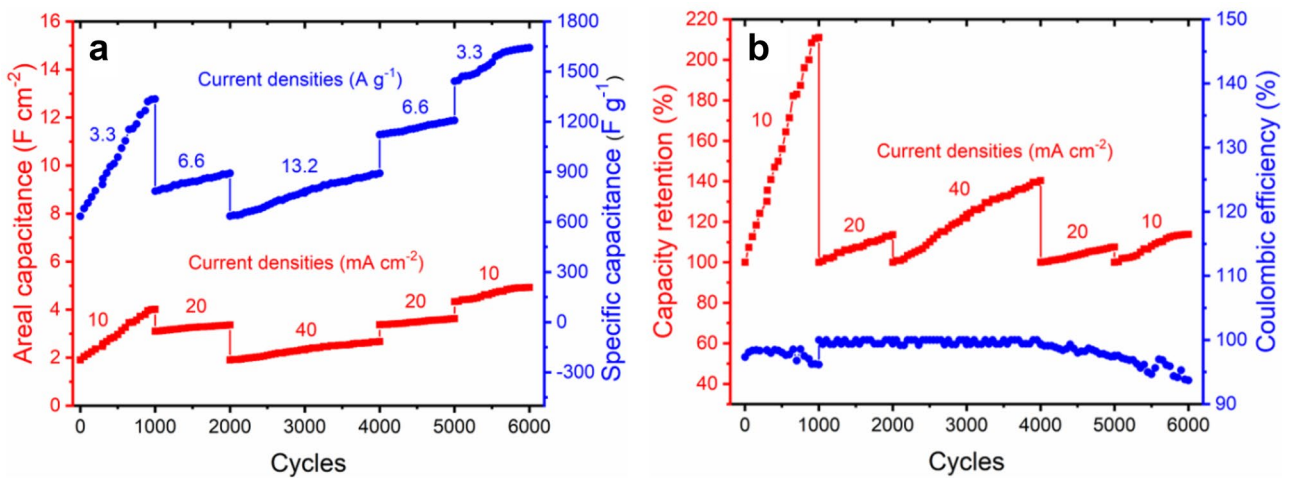

Fig. 7 **a** Areal and specific capacitance *vs*. cycles and **b** capacity retention and Coulombic efficiency vs. cycles of CoMn₂O₄ electrode

surface area, wider pore size distribution, and the larger contact area between the electrode and current collector. All these parameters improve the diffusion and surface-controlled process benefited by its high areal and specific capacitance, better rate capability, and excellent capacity retention. Comparative data for some of the recently studied $CoMn_2O_4$ electrode materials with various morphologies are given in Table 1.

Conclusion

In the present work, we followed a one-step, binder-free, surfactant-assisted hydrothermal route to prepare exquisite nanostructures with splendid structural integrity and superior capacitance. The surfactant greatly assisted the growth of nanostructures, thus resulting in beautifully decorated chrysanthemum nanoflowers on an Indian borage shrub composed of many active pores throughout the electrode material. The $CoMn_2O_4$ showed excellent pseudocapacitive properties with a high specific capacitance of 1642 F g^{-1} and an areal capacitance of 4.92 F cm^{-2} at a current density of 3.3 A g^{-1}. The outstanding cycling stability (~116% capacity retention) and a high average Coulomb efficiency of ~98% are due to the activation of many pores during the cycling process. Further, the enriched electrochemical performance and rate capability can be attributed to the attractive nanostructures with a good pore size that facilitates the free flow of electrolyte ions during the charge–discharge process. These features make $CoMn_2O_4$ spinel a potential and promising pseudocapacitive material for future energy storage applications.

Declarations

Conflict of interests The authors declare no competing interests.

References

1. Simon P, Gogotsi Y, Dunn B (2014) Where do batteries end and supercapacitors begin? Science 80(343):1210–1211. https://doi.org/10.1126/science.1249625
2. González A, Goikolea E, Barrena JA, Mysyk R (2016) Review on supercapacitors: technologies and materials. Renew Sust Energ Rev 58:1189–1206. https://doi.org/10.1016/j.rser.2015.12.249
3. Raza W, Ali F, Raza N et al (2018) Recent advancements in supercapacitor technology. Nano Energy 52:441–473. https://doi.org/10.1016/j.nanoen.2018.08.013
4. Fleischmann S, Mitchell JB, Wang R et al (2020) Pseudocapacitance: from fundamental understanding to high power energy storage materials. Chem Rev 120:6738–6782. https://doi.org/10.1021/acs.chemrev.0c00170
5. Mathis TS, Kurra N, Wang X et al (2019) Energy storage data reporting in perspective—guidelines for interpreting the performance of electrochemical energy storage systems. Adv Energy Mater 9:1–13. https://doi.org/10.1002/aenm.201902007
6. Miller JR, Simon P (2008) Materials science: electrochemical capacitors for energy management. Science 321:651–652. https://doi.org/10.1126/science.1158736
7. Srivastav S, Paliwal MK, Meher SK (2022) Ribbon-like nickel cobaltite with layer-by-layer-assembled ordered nanocrystallites for next-generation all-solid-state hybrid supercapatteries. Langmuir 38:3969–3983. https://doi.org/10.1021/acs.langmuir.1c02844
8. Gogotsi Y, Penner RM (2018) Energy storage in nanomaterials - capacitive, pseudocapacitive, or battery-like? ACS Nano 12:2081–2083. https://doi.org/10.1021/acsnano.8b01914
9. Boujibar O, Ghamouss F, Ghosh A et al (2019) Activated carbon with exceptionally high surface area and tailored nanoporosity obtained from natural anthracite and its use in supercapacitors. J Power Sources 436:226882. https://doi.org/10.1016/j.jpowsour.2019.226882
10. Sahoo MK, Ranga Rao G (2021) A high energy flexible symmetric supercapacitor fabricated using N-doped activated carbon derived from palm flowers. Nanoscale Adv 3:5417–5429. https://doi.org/10.1039/d1na00261a
11. Meher SK, Justin P, Ranga Rao G (2010) Pine-cone morphology and pseudocapacitive behavior of nanoporous nickel oxide. Electrochim Acta 55:8388–8396. https://doi.org/10.1016/j.electacta.2010.07.042
12. Samal R, Mondal S, Gangan AS et al (2020) Comparative electrochemical energy storage performance of cobalt sulfide and cobalt oxide nanosheets: Experimental and theoretical insights from density functional theory simulations. Phys Chem Chem Phys 22:7903–7911. https://doi.org/10.1039/c9cp06434f
13. Meher SK, Ranga Rao G (2012) Enhanced activity of microwave synthesized hierarchical MnO_2 for high performance supercapacitor applications. J Power Sources 215:317–328. https://doi.org/10.1016/j.jpowsour.2012.04.104
14. Wang L, Ji H, Wang S et al (2013) Preparation of Fe_3O_4 with high specific surface area and improved capacitance as a supercapacitor. Nanoscale 5:3793–3799. https://doi.org/10.1039/c3nr00256j
15. Umeshbabu E, Ranga Rao G (2016) Vanadium pentoxide nanochains for high-performance electrochemical supercapacitors. J Colloid Interface Sci 472:210–219. https://doi.org/10.1016/j.jcis.2016.03.050
16. Umeshbabu E, Rajeshkhanna G, Ranga Rao G (2014) Urchin and sheaf-like $NiCo_2O_4$ nanostructures: synthesis and electrochemical energy storage application. Int J Hydrogen Energy 39:15627–15638. https://doi.org/10.1016/j.ijhydene.2014.07.168
17. Rajeshkhanna G, Ranga Rao G (2018) High energy density symmetric capacitor using zinc cobaltate flowers grown in situ on Ni foam. Electrochim Acta 261:265–274. https://doi.org/10.1016/j.electacta.2017.12.115
18. Venkateswarlu P, Umeshbabu E, Naveen Kumar U et al (2017) Facile hydrothermal synthesis of urchin-like cobalt manganese spinel for high-performance supercapacitor applications. J Colloid Interface Sci 503:17–27. https://doi.org/10.1016/j.jcis.2017.05.007
19. Umeshbabu E, Justin P, Ranga Rao G (2018) Tuning the surface morphology and pseudocapacitance of MnO_2 by a facile green method employing organic reducing sugars. ACS Appl Energy Mater 1:3654–3664. https://doi.org/10.1021/acsaem.8b00390
20. Li Y, Zhu G, Xu X et al (2022) Embedding metal–organic frameworks for the design of flexible hybrid supercapacitors by

electrospinning: synthesis of highly graphitized carbon nanofibers containing metal oxide nanoparticles. Small Struct 3:2200015. https://doi.org/10.1002/sstr.202200015

21. Chen L, Xu X, Wan L et al (2021) Carbon-incorporated Fe_3O_4 nanoflakes: high-performance faradaic materials for hybrid capacitive deionization and supercapacitors. Mater Chem Front 5:3480–3488. https://doi.org/10.1039/d0qm00946f

22. Aparna ML, Thomas T, Ranga Rao G (2022) Battery-like super-capacitive behavior of urchin-shaped $NiCo_2O_4$ and comparison with $NiCo_2X_4$ (X = S, Se, Te). J Electrochem Soc 169:020515. https://doi.org/10.1149/1945-7111/ac4d6c

23. Aparna ML, Thomas T, Ranga Rao G (2022) Chimie douce derived nickelt cobalt oxynitride as electrode material for high energy density supercapacitors. J Electrochem Soc 418:140341. https://doi.org/10.1149/1945-7111/ac4d6c

24. Zhang C, Zheng B, Huang C et al (2019) Heterostructural three-dimensional reduced graphene oxide/$CoMn_2O_4$ nanosheets toward a wide-potential window for high-performance supercapacitors. ACS Appl Energy Mater 2:5219–5230. https://doi.org/10.1021/acsaem.9b00904

25. Ren L, Chen J, Wang X et al (2015) Facile synthesis of flower-like $CoMn_2O_4$ microspheres for electrochemical supercapacitors. RSC Adv 5:30963–30969. https://doi.org/10.1039/c5ra02663f

26. Syedvali P, Rajeshkhanna G, Umeshbabu E et al (2015) In situ fabrication of graphene decorated microstructured globe arti-chokes of partial molar nickel cobaltite anchored on a Ni foam as a high-performance supercapacitor electrode. RSC Adv 5:38407–38416. https://doi.org/10.1039/c5ra03463a

27. Luo Z, Shu D, Yi F et al (2021) Urchin-like $NiCo_2O_4$ hollow micro-spheres with oxygen vacancies synthesized by self-template for supercapacitor. New J Chem c: https://doi.org/10.1039/d1nj04153c

28. Umeshbabu E, Rajeshkhanna G, Ranga Rao G (2016) Effect of solvents on the morphology of $NiCo_2O_4$/graphene nanostruc-tures for electrochemical pseudocapacitor application. J Solid State Electrochem 20:1837–1844. https://doi.org/10.1007/s10008-015-3022-5

29. Pattanayak B, Simanjuntak FM, Panda D et al (2019) Role of precursors mixing sequence on the properties of $CoMn_2O_4$ cath-ode materials and their application in pseudocapacitor. Sci Rep 9:16852. https://doi.org/10.1038/s41598-019-53364-2

30. Sandosh TA, Simi A (2021) Morphology controlled synthesis of one-dimensional $CoMn_2O_4$ nanorods for high-performance super-capacitor electrode application. Chem Pap 75:2295–2304. https://doi.org/10.1007/s11696-020-01448-z

31. Padmanathan N, Selladurai S (2014) Mesoporous $MnCo_2O_4$ spinel oxide nanostructure synthesized by solvothermal technique for supercapacitor. Ionics (Kiel) 20:479–487. https://doi.org/10.1007/s11581-013-1009-8

32. Wu C, Cai J, Zhang Q et al (2015) Direct growth of urchin-like $ZnCo_2O_4$ microspheres assembled from nanowires on nickel foam as high-performance electrodes for supercapacitors. Electrochim Acta 169:202–209. https://doi.org/10.1016/j.electacta.2015.04.079

33. Umeshbabu E, Rajeshkhanna G, Justin P, Ranga Rao G (2015) Magnetic, optical and electrocatalytic properties of urchin and sheaf-like $NiCo_2O_4$ nanostructures. Mater Chem Phys 165:235–244. https://doi.org/10.1016/j.matchemphys.2015.09.023

34. Vigneshwaran P, Kandiban M, Senthil Kumar N et al (2016) A study on the synthesis and characterization of $CoMn_2O_4$ electrode

35. Jiang S, Shi T, Long H et al (2014) High-performance binder-free supercapacitor electrode by direct growth of cobalt-manganese composite oxide nansostructures on nickel foam. Nanoscale Res Lett 9:1–8. https://doi.org/10.1186/1556-276X-9-492

36. Yunyun F, Xu L, Wankun Z et al (2015) Spinel $CoMn_2O_4$ nanosheet arrays grown on nickel foam for high-performance supercapacitor electrode. Appl Surf Sci 357:2013–2021. https://doi.org/10.1016/j.apsusc.2015.09.176

37. Yuan C, Yang L, Hou L et al (2012) Growth of ultrathin mesoporous Co_3O_4 nanosheet arrays on Ni foam for high-performance electro-chemical capacitors. Energy Environ Sci 5:7883–7887. https://doi.org/10.1039/c2ee21745g

38. Du H, Jiao L, Wang Q et al (2013) Facile carbonaceous micro-sphere templated synthesis of Co_3O_4 hollow spheres and their electrochemical performance in supercapacitors. Nano Res 6:87–98. https://doi.org/10.1007/s12274-012-0283-5

39. Rajeshkhanna G, Umeshbabu E, Justin P, Ranga Rao G (2015) In situ fabrication of porous festuca scoparia-like $Ni_{0.3}Co_{2.7}O_4$ nanostructures on Ni-foam: An efficient electrode material for supercapacitor applications. Int J Hydrogen Energy 40:12303–12314. https://doi.org/10.1016/j.ijhydene.2015.06.046

40. Zhang L, He G, Lei S et al (2016) Hierarchical hollow microflowers constructed from mesoporous single crystalline $CoMn_2O_4$ nanosheets for high performance anode of lithium ion battery. J Power Sources 326:505–513. https://doi.org/10.1016/j.jpowsour.2016.07.021

41. Kutty RKN, Kasturi PR, Jaganath J et al (2019) Structural and magnetic properties of $CoMn_2O_4$ synthesized by auto combustion method. J Mater Sci Mater Electron 30:975–981. https://doi.org/10.1007/s10854-018-0366-5

42. Sim C, Majid SR, Zalina N (2019) Durable porous carbon/$ZnMn_2O_4$ composite electrode material for supercapacitor. J Alloys Compd 803:424–433. https://doi.org/10.1016/j.jallcom.2019.06.220

43. Saranya SPE (2018) Efficient electrochemical performance of $ZnMn_2O_4$ nanoparticles with rGO nanosheets for electrodes in supercapacitor applications. J Mater Sci Mater Electron 29:3326–3339. https://doi.org/10.1007/s10854-017-8268-5

44. Xu Y, Wang X, An C et al (2014) Facile synthesis route of porous $MnCo_2O_4$ and $CoMn_2O_4$ nanowires and their excellent electro-chemical properties in supercapacitors. J Mater Chem A 2:16480–16488. https://doi.org/10.1039/c4ta03123g

45. Cheng J, Liu X, Lu Y et al (2016) Porous $CoMn_2O_4$ microspheres as advanced pseudocapacitive materials. Mater Lett 165:231–234. https://doi.org/10.1016/j.matlet.2015.12.001

46. Meher SK, Justin P, Ranga Rao G (2011) Microwave-mediated synthesis for improved morphology and pseudocapacitance per-formance of nickel oxide. ACS Appl Mater Interfaces 3:2063–2073. https://doi.org/10.1021/am200294k